AGU PUBLICATIONS

JGR

Journal of Geophysical Research: Oceans

RESEARCH ARTICLE

10.1002/2015JC011527

Key Points:
- Rain-formed fresh lenses are modeled with the Generalized Ocean Turbulence Model (GOTM)
- Near-surface vertical salinity gradients are linearly related to rain, inversely related to wind
- In some regions, fresh lenses could cause a fresh bias between satellite and Argo salinities

Correspondence to:
K. Drushka,
kdrushka@apl.uw.edu

Citation:
Drushka, K., W. E. Asher, B. Ward, and K. Walesby (2016), Understanding the formation and evolution of rain-formed fresh lenses at the ocean surface, *J. Geophys. Res. Oceans*, *121*, doi:10.1002/2015JC011527.

Received 8 DEC 2015
Accepted 18 MAR 2016
Accepted article online 22 MAR 2016

Understanding the formation and evolution of rain-formed fresh lenses at the ocean surface

Kyla Drushka[1], William E. Asher[1], Brian Ward[2], and Kieran Walesby[2,3]

[1]Applied Physics Laboratory, University of Washington, Seattle, Washington, USA, [2]AirSea Laboratory, School of Physics and Ryan institute, National University of Ireland, Galway, Ireland, [3]Scottish Environment Protection Agency, Stirling, UK

Abstract Rain falling on the ocean produces a layer of buoyant fresher surface water, or "fresh lens." Fresh lenses can have significant impacts on satellite-in situ salinity comparisons and on exchanges between the surface and the bulk mixed layer. However, because these are small, transient features, relatively few observations of fresh lenses have been made. Here the Generalized Ocean Turbulence Model (GOTM) is used to explore the response of the upper few meters of the ocean to rain events. Comparisons with observations from several platforms demonstrate that GOTM can reproduce the main characteristics of rain-formed fresh lenses. Idealized sensitivity tests show that the near-surface vertical salinity gradient within fresh lenses has a linear dependence on rain rate and an inverse dependence on wind speed. Yearlong simulations forced with satellite rainfall and reanalysis atmospheric parameters demonstrate that the mean salinity difference between 0.01 and 5 m, equivalent to the measurement depths of satellite radiometers and Argo floats, is −0.04 psu when averaged over the 20°S–20°N tropical band. However, when averaged regionally, the mean vertical salinity difference exceeds −0.15 psu in the Indo-Pacific warm pool, in the Pacific and Atlantic intertropical convergence zone, and in the South Pacific convergence zone. In most of these regions, salinities measured by the Aquarius satellite instrument have a fresh bias relative to Argo measurements at 5 m depth. These results demonstrate that the fresh bias in Aquarius salinities in rainy, low-wind regions may be caused by the presence of rain-produced fresh lenses.

1. Introduction

Rain falling on the ocean surface produces buoyant surface "lenses" of fresher water. These surface freshening events affect salinity variability in the upper ocean and may affect calibration and validation of satellite measurements of salinity [*Boutin et al.*, 2016; *SPURS-2 Planning Group*, 2015]. Turbulence and convective overturning mix fresh lenses vertically and horizontally, causing a fresh anomaly in salinity that can extend from the surface to the base of the mixed layer. The response of the upper ocean to this freshwater input is a function of the accumulated rain, wind, net air-sea heat flux, and the background stratification and velocity of the upper few meters of the ocean. However, the relative importance of these factors in determining the fate of the freshwater input of rain is not well characterized.

In the context of understanding and improving satellite salinity validation in the rainy tropical regions, recent efforts have aimed to quantify the rain-induced vertical salinity gradients in the upper few meters of the ocean [*Henocq et al.*, 2010; *Asher et al.*, 2014; *Boutin et al.*, 2014; *Drucker and Riser*, 2014; *Santos-Garcia et al.*, 2014; *Tang et al.*, 2014; *Walesby et al.*, 2015]. Some of these studies have shown that rain on the ocean surface creates a salinity gradient between the sea surface and a few meters depth [*Boutin et al.*, 2014; *Drucker and Riser*, 2014], and that the surface freshening from an individual rain event can be large compared to the accuracy requirements for satellite salinity measurements. However, because rainfall is spatially and temporally sparse in many regions, it is still open for debate whether these rain-induced salinity gradients cause satellite salinity measurements to be slightly fresher than Argo-based measurements. What is clear is that whether or not rain-induced vertical salinity gradients affect calibration and validation of satellite salinity sensors, near-surface vertical salinity anomalies produced by rain events are relevant in measuring and understanding upper ocean salinity variability and air-sea exchange. This is especially true in regions such as the intertropical convergence zone (ITCZ) and monsoon-forced areas, where heavy rainfall is common and salinity controls upper ocean stratification. With continued improvements to satellite salinity

sensor accuracy and spatial resolution, retrieval algorithms, and data analysis techniques, using satellites to observe small-scale events such as individual rainstorms is becoming feasible [e.g., *Boutin et al*., 2014], and understanding the boundary layer salinity response to rainfall is of great interest.

The objectives of the present study are to determine how rain and wind forcing controls the thickness, stratification strength, and lifetime of fresh lenses, and to quantify the impacts of rain-formed fresh lenses on the fresh bias in satellite retrievals of salinity. In section 2, the dynamics of rain-formed lenses are described. In section 3, the Generalized Ocean Turbulence Model (GOTM) is introduced and validated with observations from two operationally distinct platforms. Statistics on the rain and wind dependence of fresh lenses are developed in section 4. In section 5, yearlong GOTM simulations are used to estimate the mean bias in satellite salinity relative to Argo due to rainfall over regional and global scales.

2. Background

In the tropics, precipitation deposits cold freshwater onto the sea surface, producing buoyant lenses of fresher water with lateral scales of O(1)–O(10) km, set by the horizontal scale of the rainfall, and vertical scales of O(0.01)–O(10) m [*Katsaros and Buettner*, 1969; *Price*, 1979; *Tomczak*, 1995; *Soloviev and Lukas*, 1996; *Wijesekera et al*., 1999; *Soloviev and Lukas*, 2006; *Reverdin et al*., 2012; *Asher et al*., 2014]. The evolution of these fresh lenses is controlled by the complex interaction of buoyancy-driven and shear-driven processes: the injection of freshwater creates a stable density stratification at the surface, which is destratified by vertical and horizontal mixing. In most cases, fresh lenses appear to disperse within a few hours through vertical mixing, lateral advection, and convectively driven overturning during nighttime cooling [*Price*, 1979; *Tomczak*, 1995; *Brainerd and Gregg*, 1997; *Wijesekera et al*., 1999]. However, rain-produced fresh lenses have also been observed to persist for tens of hours [*Walesby et al*., 2015]. Regardless of the lifetime, lateral spreading distance, or thickness of a particular fresh lens, the details of how the processes involved interact to produce its observed behavior are not well understood.

One complication is that while the evolution of rain-formed fresh lenses is determined by air-sea interaction processes, the presence of a fresh lens modulates the same processes that drive its evolution. The strong vertical stratification at the base of lenses makes them act as very thin mixed layers, trapping air-sea momentum and heat fluxes within them and suppressing the transfer of heat and momentum to deeper depths. This can cause enhanced diurnal warm layers [*Webster et al*., 1996] and surface currents [*Wijesekera et al*., 1999]. In turn, these changes to near-surface ocean properties have the potential to affect local atmospheric convection and winds. The strong stratification has also been shown to suppress near-surface turbulence dissipation beneath fresh lenses [*Smyth et al*., 1997], implying that they can reduce the downward penetration of the surface momentum flux and decouple the surface from the deeper mixed layer. In other words, although fresh lenses are relatively small, short-lived features, their local impacts on both the atmosphere and the ocean mixed layer may be substantial. Knowledge of the mechanisms responsible for the buildup and decay of fresh surface anomalies is crucial to improving air-sea dynamics in coupled ocean-atmosphere models [*McCulloch et al*., 2012], for constraining the global hydrological cycle and predicting how it will respond to a warming climate, and for modeling upper ocean dynamics in rain-dominated regimes where salinity plays an important role in setting the upper ocean stratification such as the ITCZ, Indo-Pacific warm pool, or Bay of Bengal.

Rain may also be important in satellite measurements of sea surface salinity (SSS). Calibration and validation studies of satellite-measured salinity values in rainy tropical regions have identified the presence of a fresh bias in both Aquarius and SMOS measurements (where satellite salinities are slightly fresher than in situ measurements) [*Boutin et al*., 2013; *Meissner et al*., 2014]. It is hypothesized that rain-formed vertical salinity gradients may contribute to this fresh bias because satellite instruments measure salinity at depths of a few centimeters at most, which is 2 orders of magnitude shallower than the uppermost measurement depth of Argo profiling floats (approx. 5 m) that produce the primary data set used to validate satellite salinities [*Drucker and Riser*, 2014; *Boutin et al.,* 2016]. Two recent studies have investigated whether the fresh bias is correlated with the presence of rain by comparing salinity observations from SMOS or Aquarius to nearby Argo profiles and correlating the salinity difference between the satellite and Argo, ΔS, to collocated satellite-derived rain rate, R. In tropical regions, both Boutin et al. [2014] and *Drucker and Riser* [2014] found a linear relationship between ΔS and R with a slope of approximately -0.14 to -0.20 psu $(\text{mm h}^{-1})^{-1}$. *Boutin et al.* [2014]

concluded that in the rainiest tropical regions this could produce a ΔS of up to -0.2 psu in monthly 100 $\times$ 100 km^2 pixels (a value equal to accuracy requirements of both the SMOS and Aquarius salinity missions). However, when integrating this effect at regional scale, both Boutin et al. [2014] and *Drucker and Riser* [2014] found that it cannot explain all the difference between satellite SSS and Argo SSS in rainy regions. For instance, Drucker and Riser [2014] concluded that because rain events have small spatial coverages, are infrequent, and have short persistence times, they can only be responsible for at most 0.03 psu of the observed 0.1–0.2 psu fresh bias seen in satellite-derived salinities in the 15°S–15°N tropical band.

Relatively few observations of rain-generated vertical salinity gradients exist, a result of the difficulty in making accurate salinity measurements in the upper meter of the ocean and the sparse distribution of rain events in both time and space. Recently, *Asher et al.* [2014] used a ship-based, towed surface salinity profiler (SSP) in the tropical Pacific Ocean to observe vertical salinity gradients formed in the upper 2 m in response to rainfall. Considering only the rain events for which the background stratification at the surface was stable, *Asher et al.* [2014] determined that the vertical salinity gradient between 0.1 and 0.26 m, $\Delta S_{0.3-0.1}$, has a cubic dependence on R. *Asher et al.* [2014] also found that $\Delta S_{0.3-0.1}$ is inversely related to wind speed, U, by considering four events having similar R but different U. Although *Asher et al.* [2014] demonstrated the dependence of near-surface salinity gradients on both rain and wind, they did not sample enough rain events to parameterize these relationships over a wide range of conditions. They were also unable to assess the importance of background stratification or convective overturning.

3. Model and Observations

3.1. Model Setup

The Generalized Ocean Turbulence Model (GOTM) [*Burchard et al.*, 1999; *Burchard and Bolding*, 2001; *Umlauf and Burchard*, 2003] is a one-dimensional water column model that computes solutions for the vertical transport equations of heat, salt, and momentum. It offers a flexible platform that permits the implementation of a range of turbulence closure models [*Canuto et al.*, 2001], stability functions, bulk flux algorithms, and parameterizations of the forcing parameters and wave breaking. In the work described here, a two-equation k-ϵ turbulence closure scheme with dynamic dissipation rate equations for the length scales was used. This closure scheme has been shown to perform well in studies of near-surface dynamics [*Jeffery et al.*, 2010] and upper ocean diurnal cycles [*Pimentel et al.*, 2008], and has been validated in terms of its ability to reproduce observed turbulence profiles [*Stips et al.*, 2002]. The specific configuration parameters for GOTM used here are described in Table 1. Depending on the specifics of the model run, the system was forced using either observed or idealized rain rate, R; zonal and meridional wind speeds, U_Z and U_M, respectively; solar radiation, I_S; air temperature, T_A; relative humidity, RH; barometric pressure, P_A; and cloud cover fraction, C. The initial conditions consisted of temperature, T, and salinity, S, profiles from a gridded Argo climatology [*Roemmich and Gilson*, 2009]. The shallowest Argo level is 5 m, so T and S between 0 and 5 m were set to their 5 m values, implying a well-mixed surface layer. Vertical velocity profiles of zero were used. Fluxes were computed by GOTM using the COARE (Coupled Ocean Atmosphere Response Experiment) [*Fairall et al.*, 1996] bulk flux algorithm, with the infrared radiation computed following *Clark et al.* [1974]. Absorption of solar radiation was computed according to an exponential law [see *Paulson and Simpson*, 1977], assuming Jerlov Type I water [*Jerlov*, 1976]. The model was run with a 10 s time step, a vertical domain of the upper 100 m of the water column, and a telescoping 200-layer grid having vertical spacing $<$0.05 m in the upper 2 m increasing to 1.5 m below 50 m depth. To prevent turbulent kinetic energy (TKE) dissipation from being extinguished in low-wind conditions, an internal wave breaking parameterization [*Mellor*, 1989] was used. It has been shown that including surface mixing via wave breaking can improve model representation of the upper ocean boundary layer [*He and Chen*, 2011]; here, surface wave breaking was parameterized using the model of *Burchard* [2001].

3.2. Observational Data

For the sensitivity tests and analysis of the effect of rain on satellite salinity retrievals described below, it was necessary to have data sets of meteorological forcing functions, background ocean conditions, in situ salinity observations, and satellite-derived salinity. This section discusses the sources for those data sets. Satellite salinity values and in situ salinities were obtained from the Aquarius and Argo data archives, respectively. Aquarius data (Level 2, version 4) were retrieved from the Physical Oceanography Distributed Active

Table 1. Parameters for GOTM Model Setup

Turbulence Method: Second-Order Model	
Type of second-order model	Explicit Algebraic Model with weak equilibrium
Type of equation for buoyancy variance	Algebraic equation
Type of equation for variance destruction	Algebraic equation
Coefficients of second-order model	*Canuto et al.* [2001] (version A)
Dissipative length-scale method	Dynamic dissipation rate equation
TKE equation	Dynamic k-ϵ equation
TKE equation parameters	Following *Rodi* [1987]
Boundary Conditions	
Upper and lower boundary condition for k-equation	Flux boundary condition
Upper and lower boundary condition for length-scale equation	Flux boundary condition
Type of upper boundary layer	TKE-injection (breaking waves: *Burchard and Bolding* [2001])
Type of lower boundary layer	Logarithmic law of the wall
Internal Wave Model: *Mellor* [1989]	
Critical value of TKE	1×10^{-6} m^2 s^{-2}
Critical Richardson number for shear instability	0.7
Background diffusivity for shear instability	0.005 m^2 s^{-1}
Background viscosity for internal wave breaking	0.0001 m^2 s^{-1}
Background diffusivity for internal wave breaking	1×10^{-5} m^2 s^{-1}
Turbulence Parameters	
Von Kàrmàn constant	0.4
Steady state Richardson number	0.25
Minimum TKE	1×10^{-8} m^2 s^{-2}
Minimum dissipation rate	1×10^{-12} m^2 s^{-3}
Minimum buoyancy variance	1×10^{-10} m^2 s^{-4}
Minimum buoyancy variance destruction rate	1×10^{-14} m^2 s^{-5}

Archive Center at the NASA Jet Propulsion Laboratory. Aquarius acquired data from three radiometer beams having elliptical footprints 50–80 km across. The power from each beam was sampled every 1.44 s, equivalent to ~10 km along-track ground spacing. The entire Aquarius data record (from September 2011 to May 2015; note that the mission ended in June 2015) was used, and data flagged for radio frequency interference, contamination from land, sea foam, or roughness, or navigation/pointing errors were discarded. Also used were salinity values from the Hybrid Coordinate Ocean Model (HYCOM) [*Chassignet et al*., 2007], a now-cast operational model run by the Naval Research Lab and Florida State University. HYCOM assimilates available satellite and in situ sea surface temperatures, satellite altimeter observations, and vertical T and S profiles from Argo floats, expendable bathythermographs (XBTs), and moored buoys. HYCOM experiment GLBa0.08/Expt 90.9 is interpolated to the time and location of each Aquarius swath measurement, and the surface value is included as an ancillary measurement in the Aquarius data files. Note while the HYCOM "surface" value is nominally from 1 m depth, most of the Argo and XBT measurements assimilated by HYCOM are made closer to 5 m depth and hence HYCOM salinities may represent a deeper level than 1 m. Argo profiling float data were obtained from the Argo Global Data Assembly Centre via the Coriolis data center. All delayed-mode Argo profiles from 20°S to 20°N for the same time period as the Aquarius data were selected. Only the shallowest measurement was used, and profiles were rejected if the uppermost measurement was made below 6 m depth.

Satellite and reanalysis data products were used to force yearlong GOTM simulations. Rain rate estimates came from the NOAA Climate Prediction Center morphing method (CMORPH) product [*Joyce et al*., 2004]. CMORPH is based on precipitation estimates derived from satellite microwave instruments, and uses satellite infrared imagery to interpolate and temporally propagate these rainfall estimates onto a high-resolution spatiotemporal grid. The results presented below were obtained using the 0.25° × 0.25°, 3 hourly CMORPH rain rate data for 2012. Additional meteorological forcing for the yearlong GOTM runs (U_Z, U_M, T_A, RH, P_A, and C) was obtained from the ERA-Interim global atmospheric reanalysis produced by the European Centre for Medium-range Weather Forecasting (ECMWF) [*Dee et. al,* 2011]. Six hourly fields on a 0.25° × 0.25° grid were interpolated temporally to match CMORPH. Finally, background ocean conditions for GOTM simulations were set using an optimally interpolated Argo product consisting of monthly T and S profiles on a 1° × 1° horizontal grid with 58 vertical levels [*Roemmich and Gilson*, 2009], which were interpolated spatially to the CMORPH grid.

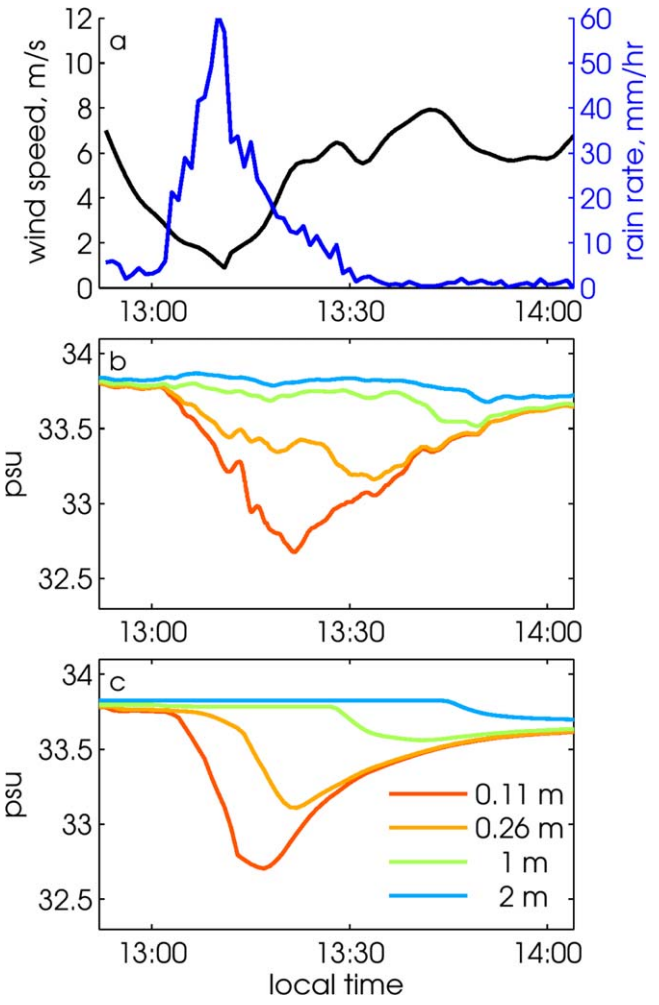

Figure 1. Observed and modeled rain event from the central Pacific Ocean. (a) Ship-based measurements of wind speed and rain rate made in 2011. (b) Salinity at four depths measured by the SSP. (c) GOTM simulation of salinity at the same four depths.

3.3. Model Validation

Although GOTM has been used for over a decade to model mixing and turbulence in the upper ocean, it has not been used to study the effects of rain in particular. The first task was therefore to validate the model using empirical data from two different rain events, each with distinct characteristics in terms of sampling strategy. One data set is a high-temporal-resolution time series from four sensors in the upper 2 m of the water column made by a towed device [*Asher et al.*, 2014] while the other is a set of high-vertical-resolution profiles made by a vertical profiler (ASIP) [*Ward et al.*, 2014]. Each data set provides unique ways to test the performance of GOTM in modeling the evolution of rain-formed fresh lenses.

The high-temporal-resolution data were collected by the SSP, which is a towed, surface-following platform that used four conductivity-temperature-depth sensors (CTDs) to sample T and S at depths of 0.11, 0.26, 1.0, and 2.0 m. Figure 1a shows the rain and wind forcing during a 4 h period measured from meteorological sensors on the *R/V Kilo Moana* as it towed the SSP through a rain storm (details concerning the SSP data are provided by *Asher et al.* [2014]). The ship was steaming northeast into the storm, which was moving in a southwesterly direction. The resulting profiles of T and S were collected from a moving frame of reference, and in order to convert them into time series that can be compared to GOTM output it is necessary to use a form of Taylor's hypothesis and assume that the measured spatial variability is equivalent to the variability that would be measured at a fixed point as a function of time. For Taylor's hypothesis to be applicable, the maximum rain rate of the storm must be constant over the time it took the ship to pass through it, and that measurement time must be fast relative to the time scale of the storm's evolution. It was not possible to directly measure the spatial structure of the storm's rain intensity as a function of time, but qualitative observations of the rain field made using the ship's navigation radar did not show significant variability in its spatial structure. This suggests that both conditions were met and that use of Taylor's hypothesis is appropriate for generating a time series from the spatial data. The SSP data are therefore used here as a function of time, where the time from the start of the rain event is computed as the distance from the maximum rain rate divided by the speed over ground of the ship.

Figure 1b shows S measured by the SSP during the rain storm. The data show that the rain rapidly produced a fresh lens having a maximum vertical salinity gradient of around 1 psu between 0.11 and 2 m. This event was modeled using GOTM, which was forced with R, U_Z, U_M, T_A, and P_A measured from the ship. C was estimated based on the difference between measured solar radiation and that predicted from the date and location, following *Reed* [1977]. The model was initiated 30 min before the onset of the rain event. Figure 1c

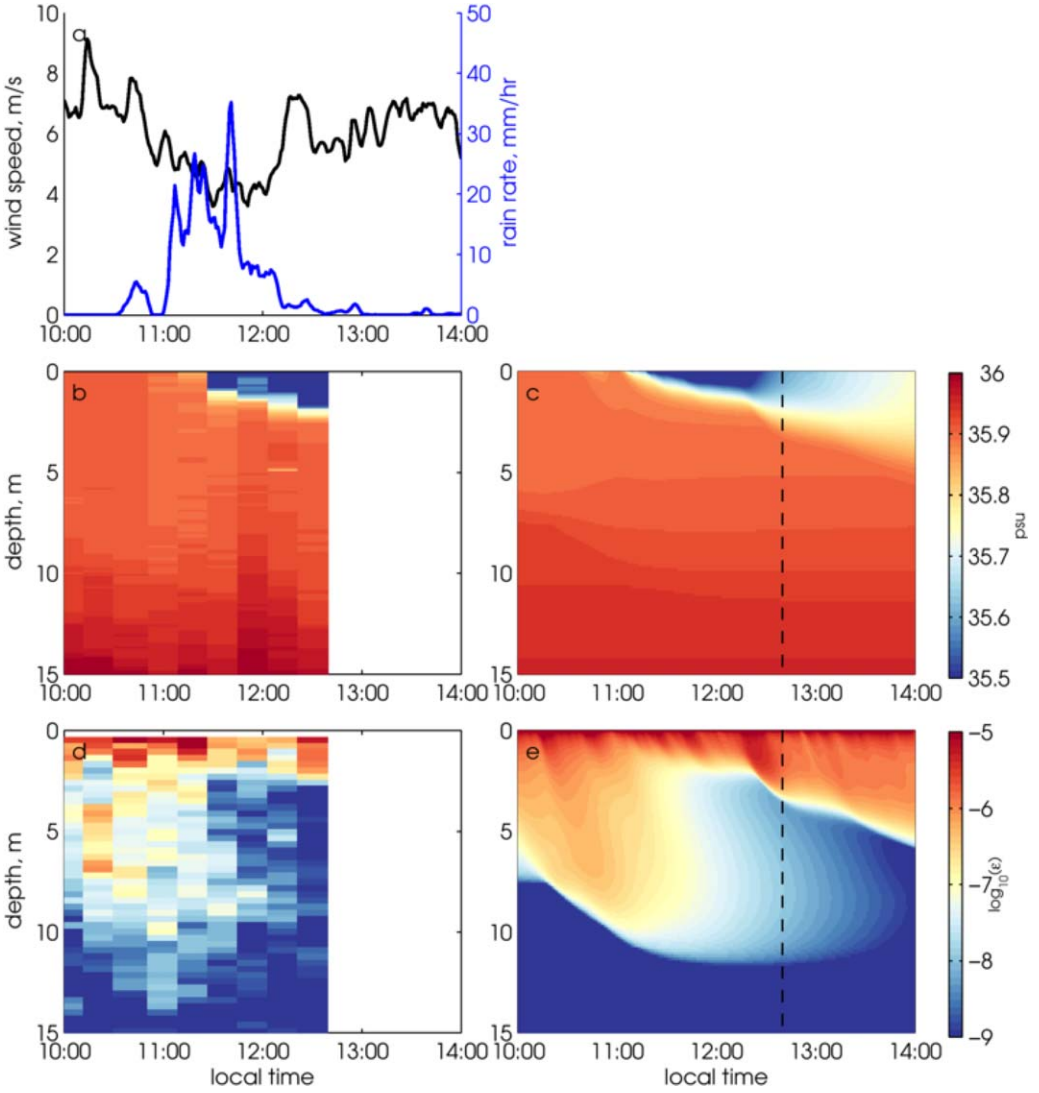

Figure 2. Rain event observed in the North Atlantic Ocean in 2011. (a) Ship-based measurements of wind speed and rain rate. (b) Salinity profiles measured by ASIP at the rate of one profile every 18 min. (c) Salinity profiles from GOTM simulations. (d) Dissipation rate profiles (log scale) measured by ASIP. (e) Dissipation rate profiles from GOTM simulation.

shows the modeled salinity at the equivalent depth levels of the four SSP sensors. GOTM reproduces the salinity response to the rain event well, including predicting the magnitude of the salinity anomaly at each depth and the erosion of the salinity gradient at the end of the rain storm. The time it takes for the fresh anomaly to propagate downward, seen as the lag between the peak salinity anomaly with depth, is also reproduced fairly well, though it occurs slightly faster in the model. The observed signal exhibits considerably more high-frequency variability than the modeled signal, likely as a result of existing variability in small-scale ocean structure or spatial/temporal variability in the rain field.

GOTM was also used to model the rain-induced surface freshening observations made by the Air-Sea Interaction Profiler (ASIP). ASIP makes upward-moving high-resolution vertical profiles of *T*, *S*, and TKE dissipation, ϵ, from below the base of the mixed layer to the sea surface [*Ward et al.*, 2014]. Figure 2 shows a rain event captured by ASIP during a 2011 deployment in the North Atlantic Ocean (40°N, 59°W) aboard the *R/V Knorr*. Meteorological measurements were made from the ship in the same region (Figure 2a). Around 20 mm of freshwater was deposited on the ocean surface during a rain event that lasted an hour, at which time the wind speed dropped to $\sim$4 m s^{-1}. ASIP captured the rapid formation of a 2 m thick fresh lens having a salinity anomaly of -0.35 psu (Figure 2b). Immediately following the

formation of the fresh lens, ϵ below 3 m depth dropped (Figure 2d), indicating that the strong stratification induced by the surface freshwater anomaly suppressed turbulence, a phenomenon also observed by *Smyth et al*. [1997]. Figures 2c and 2e show the modeled S and ϵ that result from forcing GOTM with the observed rain, wind, and other meteorological parameters beginning 30 min before the onset of the rain (Figure 2a). The model output agrees quite well with the ASIP observations, capturing the depth of the fresh lens and the time scale over which it forms. The modeled ϵ also resembles that measured by ASIP, with wind-driven mixing down to around 10 m depth that rapidly shuts off once the fresh lens forms (Figure 2e). At the time of the last ASIP profile, modeled and observed ϵ are both of order 10^{-6}, whereas within the lens (1–3 m depth), the modeled ϵ is an order of magnitude stronger than the observed ϵ.

As noted above, several different types of turbulence parameterization schemes may be used with GOTM. Sensitivity tests done as part of this validation study showed that the results presented above were largely insensitive to the surface and internal wave breaking schemes and the details of the structure function used [*Mellor and Yamada*, 1982; *Kantha and Clayson*, 1994; *Cheng et al*., 2002], although omitting the internal or surface wave breaking parameterizations resulted in slightly smaller ϵ, causing slightly ($<$10%) stronger and longer-lasting fresh lenses. Similarly, results were not sensitive to the choice of time step, domain depth, or vertical grid spacing, within a reasonable range of values. Finally, in the ocean, lateral advection and mixing contribute to the evolution of freshwater lenses [*Soloviev et al*., 2015], particularly at their edges where the horizontal gradients in T and S are largest and cause density-driven dynamical effects [*Soloviev et al*., 2002]. However, the SSP and ASIP validation efforts demonstrate that a one-dimensional model can be an appropriate tool for understanding the dynamics of freshwater lenses when horizontal currents are weak and the size of the lens is large enough that edge effects are not dominant.

3.4. Comparison to Long-Term Field Observations

GOTM-modeled fresh events were also compared to data from a mooring deployed in the Atlantic Ocean at 24.5°N, 38°W as part of the first Salinity Processes in the Upper Ocean Regional Study (SPURS) [*Lindstrom et al*., 2015]. The SPURS central mooring was equipped with rain, wind, and meteorological sensors measuring R, T_A, RH, P_A, and I_S; CTDs at numerous depths, the shallowest of which are at 0.86 and 2.1 m; and current meters, all collecting 1 min data (see *Farrar et al*. [2015], for details). During the yearlong deployment period, around 200 rain events were recorded, providing a large data set that can be used to study the dependence of vertical salinity gradients on R and U. For each rain event, the difference in salinity between the CTDs at 0.86 and 2.1 m, $\Delta S_{2.1-0.9}$, was computed, and its maximum absolute value, ΔS_{max}, was used as a metric for the strength of the vertical salinity gradient formed by that rain event. R_{max} was defined as the peak R during a given rain event. In order to facilitate comparison with GOTM, 25 rain events for which the near-surface currents (as measured using the current meter at 3 m depth) were stronger than 0.25 m s^{-1} were excluded from the analysis. This was done because in these cases horizontal advection is likely to be important so the assumption of one-dimensional dynamics may not be valid. Thirty events for which $\Delta S_{max} < 0.002$ psu were also excluded, as this represents the detection limit for salinity differences between two CTDs. This left 134 rain events, for which ΔS_{max} was determined from $\Delta S_{2.1-0.9}$. Figure 3a shows ΔS_{max} plotted as a function of U, colored by R_{max}, for the rain events observed at the SPURS mooring. The SPURS data show considerable scatter, but the results suggest that there is an inverse relationship between ΔS_{max} and U and that ΔS_{max} increases with R_{max}. As will be shown in the next section, this qualitative analysis of the SPURS results is consistent with quantitative relationships between ΔS_{max} and U and R_{max} derived from sensitivity studies.

The rain events observed at the SPURS mooring were also modeled individually: each event was forced using meteorological forcing observed from the SPURS buoy starting 2 h prior to the rain event and continuing for 2 days. Model salinity output at 0.86 and 2.1 m was extracted to form $\Delta S_{2.1-0.9}$, and the resulting modeled ΔS_{max} from each rain event is compared against the ΔS_{max} observed for that rain event (Figure 3b). There is generally good agreement between the observed and modeled salinity differences at the SPURS mooring ($R = 0.91$, significant above the 99% level), and there is no systematic bias between GOTM and the field data.

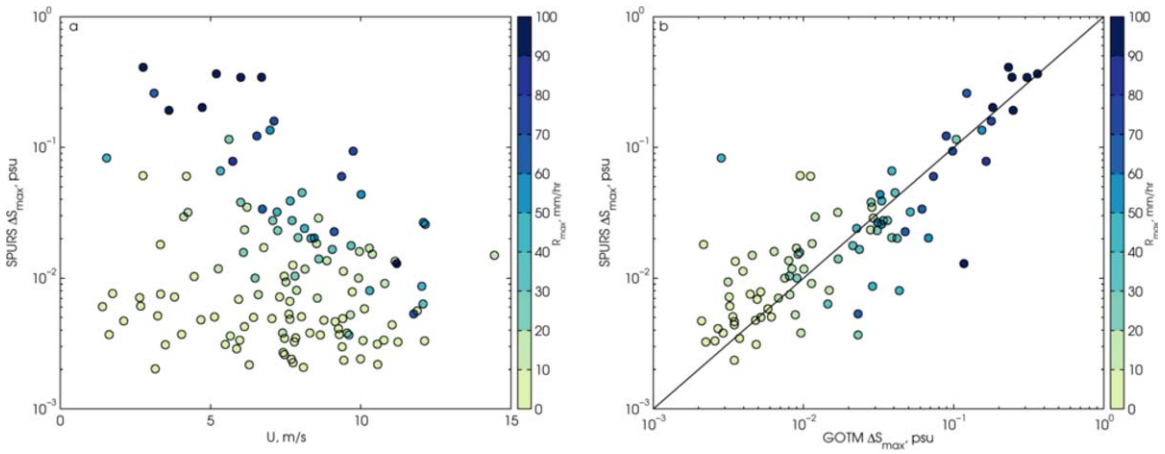

Figure 3. (a) ΔS_{max} between 0.86 and 2.1 m as a function of wind speed for events observed at the SPURS mooring in the subtropical North Atlantic Ocean; (b) observed versus modeled ΔS_{max} for rain events at the SPURS mooring. In both plots, datapoints are colored as a function of R_{max}.

4. Model Sensitivity Experiments

Once it was determined that GOTM is able to simulate the upper ocean response to rainfall, numerical experiments were performed to understand how rain intensity, wind forcing, and background ocean conditions affect the formation and evolution of fresh lenses. These numerical experiments were initialized with ocean conditions from the SSP deployment (see Figure 1). The model was forced with constant winds and a Gaussian pulse of rain having a prescribed R_{max}. Each rain pulse was 1 h long (defined using the full width of the Gaussian at one tenth of the peak) and peaked at 09:00 local time. U and R_{max} were varied between different experiments. The sensitivity experiments were run with R_{max} ranging from 2 to 100 mm h^{-1} and U ranging from 1 to 10 m s^{-1} (U was constant over the duration of the simulation, with zonal and meridional components set to the same value ($\sqrt{2}$)). After initialization, the model was not relaxed to prescribed conditions, but ran for a 2 day time period without readjustment. As was done for the validation cases, there were 200 vertical levels over a 100 m domain depth, and a 10 s time step was used. T_A, RH, and P_A were held fixed using the average values from the SSP observations for the entire 2 day period and a constant value for C of 100% was used. Although in real-world scenarios each of these parameters exhibits periodicity on diurnal, semidiurnal, and higher-frequency time scales, using constant values allows study of the ocean response that is directly due to rainfall. Initial T and S profiles came from the gridded Argo data set at the location the SSP measurements were made, and were shifted to match the mean surface T and S observed with the SSP. This was done to ensure that the air temperature, pressure, and humidity, and hence the rain temperature computed by the model, were consistent with the local sea surface temperature (SST). Solar radiation was not prescribed, but was calculated by GOTM based on the latitude, time of day, and cloud cover. Because solar heating follows a diurnal cycle, there was a diurnal cycle in upper ocean temperature. In order to separate the rain-induced anomalies from effects of the diurnal temperature cycle, as a control the model was run at each wind speed with rain set to zero at all times.

Figure 4 shows an example of the idealized forcing and the modeled ocean response. Immediately following the onset of rainfall, a surface lens of fresher water forms. Several metrics have been defined in order to characterize the ocean response to rain forcing and simplify intercomparison of model runs. The thickness of the lens, D_L, is defined as the depth at which the salinity anomaly relative to the no-rain control run is 10% of the maximum anomaly (black line in Figure 4b). The lifetime of the lens, T_L, is the time over which D_L is nonzero. Finally, in order to relate the model findings to satellite-Argo salinity comparisons, the difference in S between 0.01 m (i.e., roughly the depth of L-band satellite measurements) and 5 m (i.e., roughly the depth of the uppermost Argo measurements) was calculated at each time step. This salinity difference is defined here as ΔS, the 5 m salinity subtracted from the 0.01 m salinity so that a surface freshening will have a negative value of ΔS (Figure 4c). For each fresh lens time series, ΔS_{max} is defined as the absolute value of the largest-in-magnitude negative value of ΔS observed over the interval defining T_L, so that ΔS_{max} has a positive value.

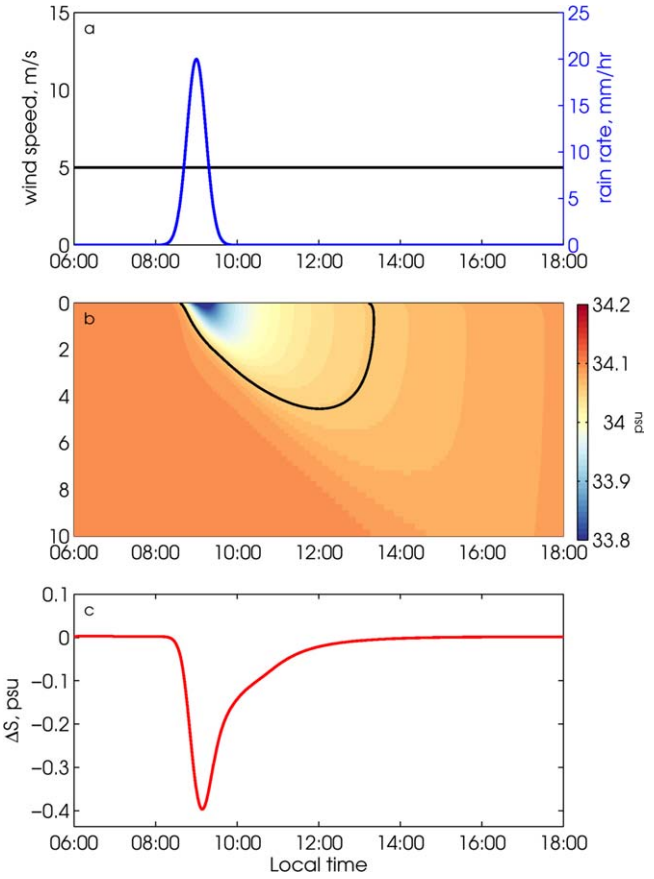

Figure 4. Example of a GOTM simulation used for the sensitivity tests using idealized forcing functions. (a) The wind (black) and rain (blue) forcing. (b) Salinity in the upper 10 m. The thick black line indicates the depth of the fresh lens, D_L, determined as the depth at which the salinity anomaly relative to the no-rain control case is 10% of its maximum value. (c) Vertical salinity gradient, ΔS, computed as the difference between salinity at 0.01 and 5 m depth.

4.1. Rain and Wind Dependence of Rain Lenses

The results from the sensitivity runs are summarized in Figure 5. Unsurprisingly, rainstorms with larger R_{max} produce stronger vertical salinity gradients having larger values of ΔS_{max}. Figure 5a shows results from simulations at three values of U. The results demonstrate that for a given U, ΔS_{max} has a nearly linear dependence on R_{max}. Figures 5b–5d show that at a given R_{max}, ΔS_{max} and T_L are inversely related to U and that D_L is linearly proportional to U. The physical explanation of these results is that stronger winds drive stronger mixing, which quickly deepens (thickens) the fresh lens, increasing D_L, but reduces the magnitude of ΔS_{max}. Vertical salinity gradients formed under strong winds are characterized by small ΔS_{max}, large D_L, and T_L of a few hours at most. In contrast, rainfall during weak winds produces a fresh lens with a large ΔS_{max}, small D_L, and T_L on order of 10 h.

Based on the results in Figure 5, it was assumed that a linear relationship between ΔS_{max} and R_{max} exists at each U. By performing a least squares linear regression of ΔS_{max} with respect to R_{max} at each U, it emerges that the slope of each line is inversely proportional to U. These slopes can then be fitted to a power law so they may be predicted as a function of U. Thus, ΔS_{max} can be parameterized as a function of both R_{max} and U:

$$\Delta S_{\max} = A R_{\max} U^{-b}, \tag{1}$$

where A and b are scalars determined from the fitting procedures. Using all GOTM runs, with the background ocean and atmosphere conditions from the central Pacific Ocean, these coefficients were found to be $A = 0.11 \pm 0.03$ psu (mm h^{-1})$^{-1}$ and $b = 1.1 \pm 0.03$. This is close to the results of both Drucker and Riser [2014], who found a value of $A = 0.14$ psu (mm h^{-1})$^{-1}$ averaged over the tropics, and *Boutin et al.* [2014], who found values of A ranging from 0.14 to 0.22 psu (mm h^{-1})$^{-1}$ at moderate wind speeds depending on the region. However, neither study considered the dependence on U separately. The slightly stronger values of A found by Drucker and Riser [2014] and *Boutin et al.* [2014] compared to the GOTM value may be due to the fact that the former use satellite measurements, which are integrated over a pixel that may not be entirely covered by rain.

The maximum thickness of rain lenses, D_L, has a roughly linear relationship with U, but the slope of the linear fit is a function of R_{max} (Figure 5c). When $R_{\max} \geq 50$ mm h^{-1}, events for which a large amount of freshwater is deposited on the ocean surface, the scale factor between U and D_L is approximately 0.8 h so that a U of 10 m s^{-1} forms an 8 m thick fresh lens after a few hours. However, at lower R_{max}, the scale factor between U and D_L is approximately 0.3 h, and there appears to be an upper limit for D_L of a few meters. The upper limit in D_L at low rain rates likely occurs because there is not enough freshwater to produce a

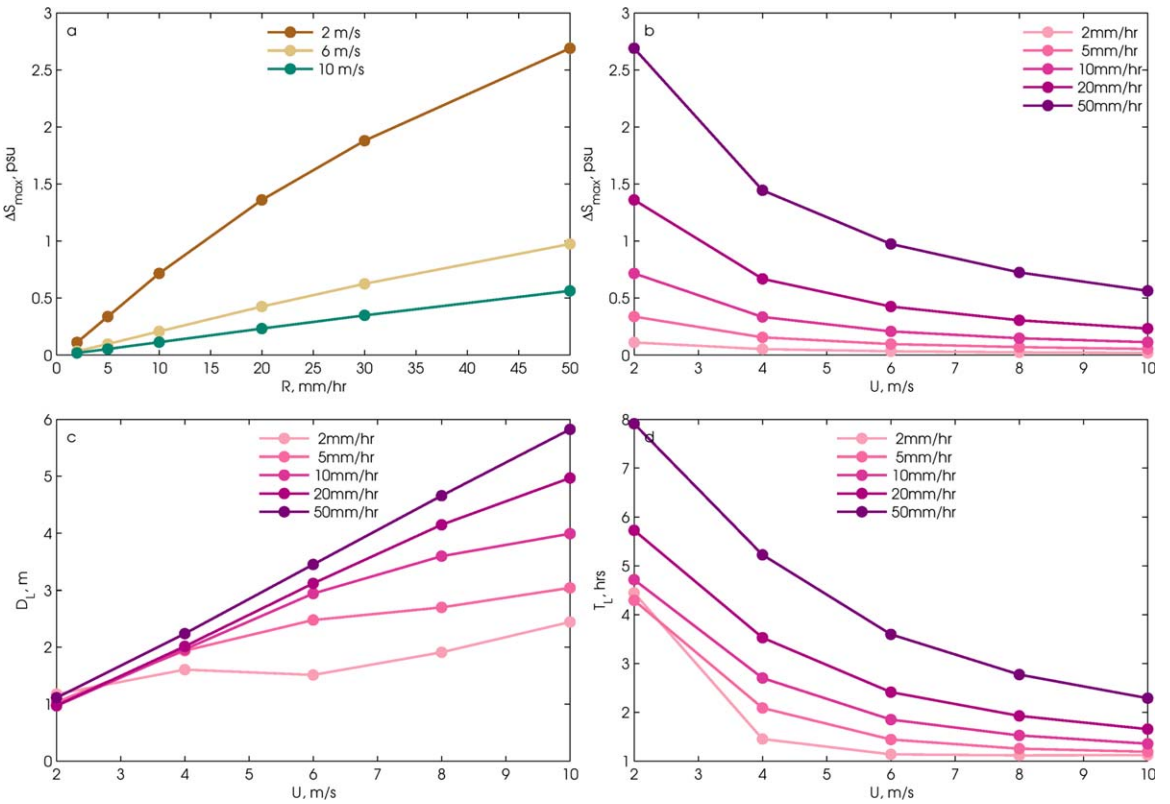

Figure 5. Results from the GOTM experiments using idealized environmental forcing functions in which the peak rain rate and the wind speed were varied. (a) Peak magnitude of ΔS, ΔS_{max}, as a function of rain rate, for three different wind speeds; (b) ΔS_{max} as a function of wind speed, for different rain rates; (c) maximum thickness of the fresh lens, D_L, as a function of wind speed at different rain rates; and (d) lifetime of the fresh lens, T_L, as a function of wind speed at different rain rates.

detectable thicker lens. Figure 5d shows T_L as a function of U. For a given R_{max}, low wind conditions result in slower mixing and a more persistent lens. For example, when $R_{max} = 50$ mm h^{-1}, $T_L = 8$ h for $U = 2$ m s^{-1}. In contrast, $T_L = 2.5$ h for $U = 10$ m s^{-1}. At constant U, smaller values for R_{max} result in smaller T_L, as the lens disperses more quickly when less freshwater is deposited.

Figure 5 uses R_{max} as the metric to describe rain events. However, it is possible that total rainfall accumulation, as opposed to R_{max}, drives the salinity response. To address this question, a series of GOTM experiments were performed where the model was forced with simulated rain events having the same total accumulated rainfall amount (0.01 m), but a different rain duration (ranging from 30 min to 6 h), and hence a different R_{max}. Although all events in Figure 6 were forced with the same total volume of rainfall, the salinity anomalies vary widely and are clearly related to R_{max}. Interestingly, T_L is approximately the same for each event, which suggests that if the presence or absence of a fresh lens is important (e.g., when considering the reduction of turbulence below the lens), the accumulated amount of freshwater is critical. In contrast, when considering rain impacts that are related to the strength of the salinity gradient (e.g., the impact on satellite-Argo salinity bias), R_{max} is a more important metric than the rain accumulation.

The effect of a non-Gaussian temporal distributions of rain was also studied by running simulations where R was a constant value for a finite length of time (e.g., 1 h). Although the resulting rain lenses had a slightly different shape in comparison to the lenses formed using Gaussian rain pulses, ΔS_{max} had a similar relationship to U and R_{max} as it did for the hour-long Gaussian rain cases shown in Figure 5. This suggests that it is R_{max}, rather than the duration of the rain event or temporal profile of R, that determines ΔS_{max}. It should also be noted that the idealized fresh lenses considered here are all forced with rain occurring in midmorning, when the near-surface ocean tends to be stable under the influence of incoming solar radiation. Fresh lenses formed by rainfall at different times of day will have different characteristics, as noted by *Webster et al.* [1996].

Asher et al. [2014] used data from a towed profiler to quantify the relationship between $\Delta S_{0.3-0.1}$ and R and found that $\Delta S_{0.3-0.1} \sim R^3$. In contrast, GOTM results (Figure 5a) suggest a linear relationship between ΔS and

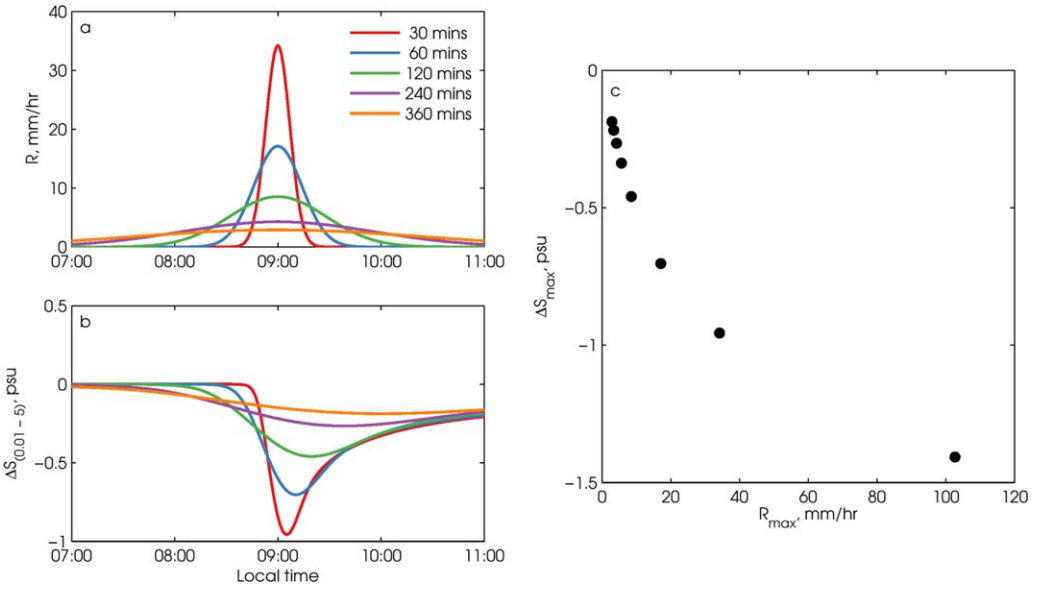

Figure 6. Results from GOTM experiments using idealized environmental forcing in which the same total rainfall accumulation of 0.01 m was applied, but the time over which it was applied varied in each case (indicated in the legend). (a) Rain rate as a function of time; (b) ΔS between 0.01 and 5 m as calculated from the GOTM simulations for the rain rate time series in Figure 6a; (c) ΔS_{max} plotted as a function of R_{max} for all conditions.

R_{max}, appearing to contradict *Asher et al*. [2014]. (Note that although Figure 5 shows ΔS calculated between 0.01 and 5 m, if $\Delta S_{0.3-0.1}$ is calculated using the GOTM results, it also shows a linear relationship with R_{max}, albeit with different coefficients.) There are several possible explanations for this discrepancy. First, the model has allowed estimation of ΔS for all possible rain and wind combinations, whereas the observations of *Asher et al*. [2014] span a very small subset of combinations. For example, *Asher et al*. [2014] never observed high R and high U and therefore could not consider the dependence of $\Delta S_{0.3-0.1}$ on R at different U. Second, *Asher et al*. [2014] did not develop their relationship using R_{max}, but instead used the R that was present when $\Delta S_{0.3-0.1}$ was at its maximum value for that rain event. As seen in Figure 1, because it takes a finite amount of time for the salinity gradient to develop and reach ΔS_{max}, the rain rate measured at that time is not the maximum rain rate. Third, the model is an idealized one-dimensional case in which advection is ignored and it is possible that advection was nonnegligible in some of the cases observed by *Asher et al*. [2014].

Additional sensitivity experiments were performed to explore how different upper ocean temperature and salinity conditions affect ΔS_{max} (not shown). At a given surface temperature, the near-surface salinity anomaly resulting from rainfall is proportional to the initial surface salinity, as could be expected from linear dilution. Therefore, rain falling on saltier water produces a stronger vertical salinity gradient than rain on fresher water. At a fixed surface salinity, the impact of SST on ΔS_{max} was found to be small, with the magnitude of ΔS_{max} decreasing slightly with increasing temperature.

5. Implications of Rain-Formed Fresh Lenses for Satellite Validation

Previously, Boutin et al. [2014] and *Drucker and Riser* [2014] compared satellite and Argo salinity measurements as a function of R to determine if rain-induced vertical stratification between the surface and a few meters causes a fresh bias between satellite-derived and Argo-derived salinities. Although these studies are limited by the relatively sparse spatial and temporal overlap between Argo profiles and satellite overpasses, each suggests that there is a fresh bias during individual rain events. However, *Drucker and Riser* [2014] suggest that rain events may be too infrequent to cause a significant fresh bias in the long-term average. GOTM-simulated near-surface salinity profiles allow a more detailed study of the prevalence of rain-induced salinity gradients to be conducted, from which the rain-induced fresh bias in long-term average satellite salinity can be deduced.

Rain-generated salinity gradients were estimated by running yearlong GOTM simulations on a 0.5° × 0.5° grid from 20°S to 20°N using a 5 min time step (which was found to perform equivalently over yearlong simulations to the 10 s time step used in the studies discussed above). Rain at each grid point was given by the 0.25° × 0.25°, 3 h CMORPH rain rate product, which was interpolated to the 5 min time step of the model. Time series of ocean surface wind vectors RH, T_A, P_A, and C at each location were taken from the 0.25° × 0.25°, 6 h averaged ERA-Interim product. Solar radiation was calculated by GOTM based on the latitude, time of day, and cloud cover. As was done for the CMORPH rain product, the ERA-Interim data were interpolated to match the 5 min time step of the model. To compensate for numerical drift and unresolved oceanic processes such as lateral advection and mixing, the model was relaxed to local Argo climatological T and S profiles with a 7 day relaxation time scale.

At each grid point, GOTM was run for 1 January to 31 December 2012 using the CMORPH and ERA-Interim data as the forcing. This produced a yearlong time series of the salinity profile through the mixed layer. From these profiles, a time series for ΔS between 0.01 and 5 m was calculated at each horizontal grid point, and the annual average value of the salinity difference at each grid point, $\overline{\Delta S}_{mod}$, was calculated (note that the signed character of ΔS is retained in $\overline{\Delta S}_{mod}$, so that a negative value represents a surface freshening). Figure 7a shows the resulting spatial distribution of $\overline{\Delta S}_{mod}$. The model results show strong spatial variability in the vertical salinity difference between the surface and 5 m. Average surface freshening is around 0.2 psu in the eastern equatorial Indian Ocean and western Pacific warm pool. The surface freshening is somewhat weaker throughout the Pacific and Atlantic ITCZ bands, ranging from 0.15 to 0.2 psu, and 0.1 psu in the South Pacific convergence zone (SPCZ) and in the central equatorial Indian Ocean. All of the regions with large freshening (i.e., $\overline{\Delta S}_{mod} < -0.1$ psu) are characterized by strong annual-mean rainfall (>1.5 mm h^{-1}; Figure 7b) and weak winds (<4 m s^{-1}; Figure 7c). As might be expected, $\overline{\Delta S}_{mod}$ is near zero in low-rain and high-wind regions such as the western Indian Ocean, in the Pacific and Atlantic north of 10°N, and in the South Pacific (east of 180°E) and the entire south Atlantic Ocean.

It is clear that the model results here represent a simplified system, since horizontal processes have been neglected. In the presence of surface currents, horizontal advection will disperse the fresh lens, reducing T_L and $\overline{\Delta S}_{mod}$. Because horizontal effects are not considered in the present analysis, $\overline{\Delta S}_{mod}$ in Figure 7a may overestimate the actual fresh bias observed by a satellite when compared to Argo data from 5 m. The potential magnitude of this overestimation was simulated by performing an additional experiment in which the model was relaxed to the background salinity profile once every 6 h (instead of once a week), which is effectively equivalent to having every fresh lens mixed away after 6 h at most. This resulted in a reduction of the surface freshening by around 50%, so that $\overline{\Delta S}_{mod}$ became approximately −0.1 psu in the western Pacific Ocean, eastern Indian Ocean, and ITCZ regions, with similar fractional changes in $\overline{\Delta S}_{mod}$ in other regions.

Tropical rain events are often brief and can have strong peaks. Similarly, wind speed also varies on short time scales and can drop during the time that rain is strongest (e.g., Figures 1a and 2a). The simulations conducted to produce Figure 7a, which were forced with 3 hourly rain and 6 hourly winds, therefore neglected the effects of high-frequency rain and wind variability. Figure 5 suggests forcing the model with an unrealistically low rainfall or strong wind speed would produce unrealistically weak vertical salinity gradients. To test the impact of using relatively coarse rain and wind forcing to estimate $\overline{\Delta S}_{mod}$, GOTM simulations were performed using high-frequency forcing from a Tropical Atmosphere Ocean (TAO) mooring in the western Pacific Ocean at 0°N, 165°E. Ten minute R, U_Z, U_M, RH, T_A, and P_A observations were used to force GOTM, using the same parameters as were used for the satellite-forced and reanalysis-forced simulations (Table 1). C, not measured at the mooring, was set to a constant value of 1. The model was relaxed to T and S profiles from the gridded Argo climatology using a 7 day time scale. Yearlong simulations (July 2006 to June 2007) were performed with the 10 min TAO data, producing a mean vertical salinity gradient $\overline{\Delta S}_{TAO10m}$ of −0.2 psu (not shown). A second simulation was performed using the same 10 min data TAO data that had been subsampled to a 3 h time step (after first applying a 3 h low-pass filter): this produced a mean vertical salinity gradient $\overline{\Delta S}_{TAO3h}$ of −0.03 psu. These results suggest that using forcing fields that do not capture the high-frequency fluctuations of rainfall underestimate the average vertical salinity gradient. However, it should also be noted that the model run forced by CMORPH and ERA-Interim at 0N, 165E (Figure 7a) produced a $\overline{\Delta S}_{mod}$ value of −0.13 psu, relatively close to the result

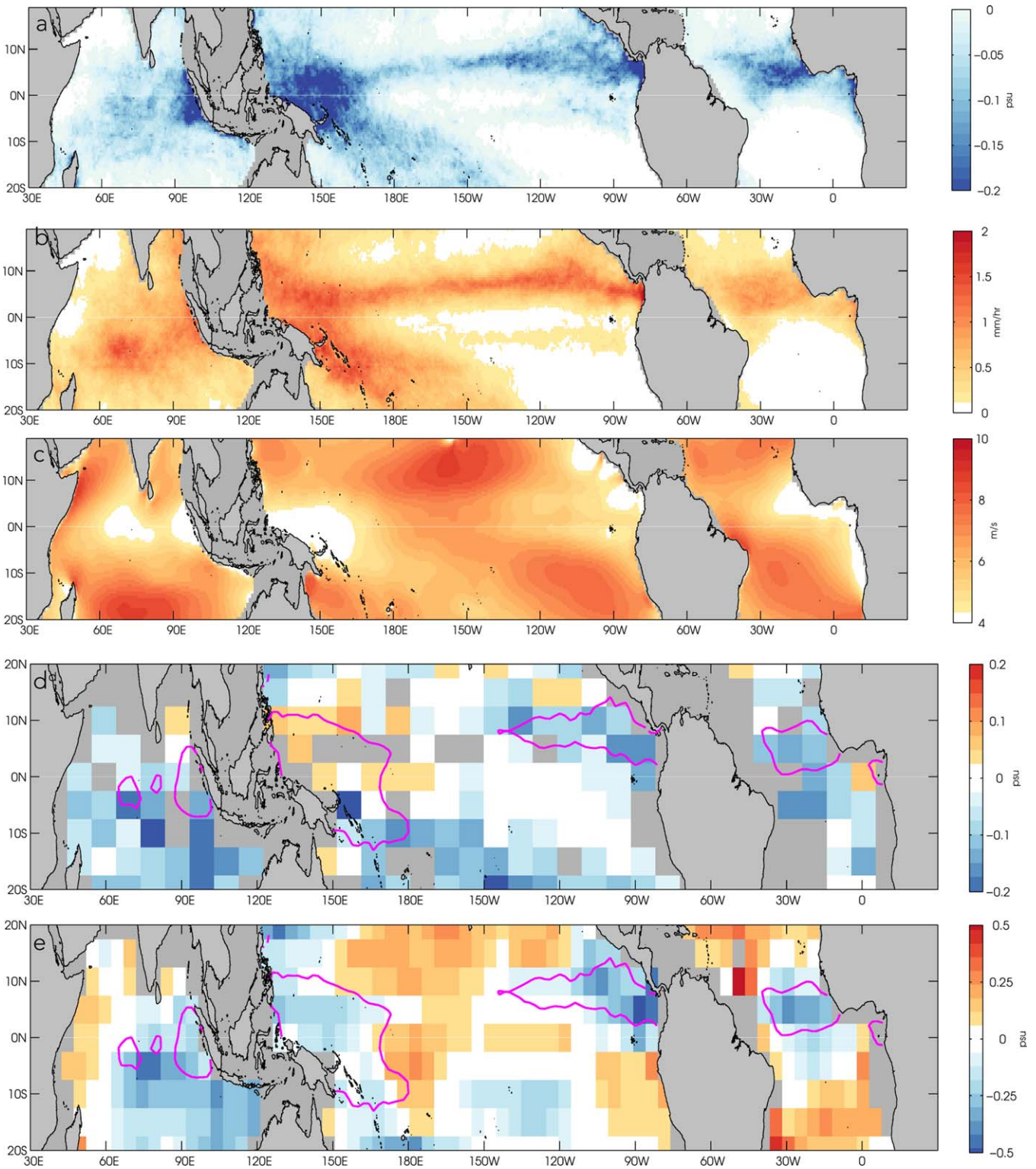

Figure 7. (a) $\overline{\Delta S}_{mod}$, the annual average of ΔS between 0.01 and 5 m, calculated from GOTM experiments run at each grid point for a 0.5° × 0.5° grid. (b) Mean rain rate, based on CMORPH precipitation estimates from 2012 on the same grid as Figure 7a. (c) Mean wind speed, based on ERA-Interim winds from 2012. (d) $\overline{\Delta S}_{obs}$, the average difference between salinity from Aquarius and from Argo at 5 m (negative indicates that Aquarius measures a fresher value). Individual Aquarius-Argo pairs were averaged to a 10° longitude × 5° latitude grid. (e) $\overline{\Delta S}_{hyc}$, the average difference between Aquarius and HYCOM salinity at 1 m depth. The pink line in Figures 7d and 7e is the 0.08 psu contour of $\overline{\Delta S}_{mod}$ from Figure 7a.

using the 10 min forcing from the TAO mooring. The reasons why $\overline{\Delta S}_{mod}$ (with 3 h averaged rainfall) is in better agreement with $\overline{\Delta S}_{TAO10m}$ than with $\overline{\Delta S}_{TAO3h}$ are not clear. One difference between the CMORPH data set and the 3 h averaged TAO data is that the CMORPH data set is produced by averaging both spatially and temporally. In contrast, only temporal averaging is possible with the TAO data, so the spatial variability in the rain field is not included in the resulting 3 h averages. A rain event with high spatial variability might be completely absent in the TAO data record if it occurred away from the point-measuring rain gauge on the buoy, whereas that same rain event would be detected in the spatially averaged CMORPH product. Complete study of how temporal averaging of rain data collected at a point versus spatiotemporal averaging of mapped rain fields impact the formation of fresh lenses (as modeled using GOTM) is beyond the scope of the present study and will require detailed exploration with three-dimensional ocean models.

Because the depth range over which $\overline{\Delta S}_{mod}$ is calculated is the same as the measurement depths of Argo and L-band radiometric salinity sensors, it is reasonable to conclude that it represents the long-term average fresh bias that would be observed between Argo and Aquarius (or SMOS) if horizontal mixing processes do not affect the fresh lenses. However, even if horizontal mixing processes are significant, the spatial pattern for $\overline{\Delta S}_{mod}$ should be similar to the spatial pattern of the difference between Aquarius and Argo. Figure 7d shows the mean observed difference between Aquarius-derived and Argo-derived salinities, $\overline{\Delta S}_{obs}$. $\overline{\Delta S}_{obs}$ was estimated by matching individual Argo profiles to Aquarius measurements where the following criteria were met: the Argo float surfaced within 50 km of the center of the satellite footprint and within $\pm$1 day of the satellite overpass. Then, for each matched pair, the Argo salinity profile was interpolated vertically to give the salinity at 5 m depth, and this value was subtracted from the Aquarius salinity. For the 20°S–20°N tropical band considered here, this resulted in 9387 Argo-Aquarius pairs covering the time period from September 2011 to May 2015. This does not produce a dense spatial distribution of data pairs, so the data were bin averaged into 10° longitude $\times$ 5° latitude grid boxes to reduce noise. Grid cells containing fewer than 15 matched pairs were excluded from further analysis.

Figure 7d shows that Aquarius salinities are up to 0.1 psu fresher than 5 m Argo salinities in the eastern Pacific and Atlantic ITCZ, and 0.1–0.2 psu fresher in the SPCZ region and throughout the tropical Indian Ocean outside of the Bay of Bengal. Aquarius salinities also are fresher in the central Pacific Ocean south of 10°S. However, Aquarius has a salty bias in the western equatorial Pacific Ocean. Direct quantitative comparison of $\overline{\Delta S}_{mod}$ and $\overline{\Delta S}_{obs}$ is not particularly helpful, but qualitatively there is some agreement between where the model predicts a fresh bias should be observed and where one is seen in the observations. This is encouraging, suggesting that the model is reproducing at least some of the relevant physics in surface freshening. However, it is not clear if differences between $\overline{\Delta S}_{mod}$ and $\overline{\Delta S}_{obs}$ are due to problems in the model or the relative paucity of observational data leading to undersampling of the surface freshening, or if they could result from interannual variations that are represented in the observations but not by the year-long model run.

Better spatial resolution in the satellite observational data can be obtained by computing the salinity difference between the Level 2 Aquarius data and the HYCOM (at 1 m depth) salinities at each Aquarius measurement location that are included as an ancillary field in the Aquarius data files. The mean Aquarius-HYCOM salinity differences, $\overline{\Delta S}_{hyc}$, were binned into 5° $\times$ 5° grid boxes and the resulting spatial distribution is shown in Figure 7e. The spatial pattern is similar to the spatial pattern for $\overline{\Delta S}_{obs}$, with fresh values in the Indian Ocean away from the western Indian and Bay of Bengal, and in the ITCZ and SPCZ regions. However, $\overline{\Delta S}_{hyc}$ is distinctly negative, and therefore fresher, in the western Pacific warm pool, whereas $\overline{\Delta S}_{obs}$ is weakly positive (+0.05 psu). In addition, the Aquarius bias relative to HYCOM is about a factor of 2 larger than the bias relative to Argo. The reasons for this difference are not clear, but the spatial pattern of $\overline{\Delta S}_{hyc}$ provides a much better match to $\overline{\Delta S}_{mod}$, suggesting that poor spatial statistics is part of the reason for the disagreement between $\overline{\Delta S}_{mod}$ and $\overline{\Delta S}_{obs}$.

Figure 7 suggests that vertical salinity gradients caused by rain-induced fresh lenses are potentially responsible for the observed fresh bias in Aquarius in certain regions. In the eastern Pacific and Atlantic ITCZ, the SPCZ, and the eastern Indian Ocean west of Sumatra, the observed Aquarius fresh bias relative to Argo is 0.1–0.2 psu (0.2–0.4 psu relative to HYCOM). The mean fresh bias predicted with GOTM is up to 0.2 psu west of Sumatra and in the Atlantic and Pacific ITCZ bands. Even considering the estimated 50% reduction in the

GOTM-derived salinity gradient due to unresolved horizontal advection, the magnitude of the modeled gradients is similar to that of the observed bias. Particularly striking is the agreement in the spatial overlap between $\overline{\Delta S}_{mod}$ and the Aquarius-HYCOM comparison (pink contour and blue shading in Figure 7e). There are also regions for which $\overline{\Delta S}_{mod}$ and the Aquarius bias are not consistent: in the Indian Ocean south of 10°S, Aquarius shows a strong fresh bias compared to both Argo and HYCOM, but the presence of rain-induced salinity gradients here is unlikely, as rain is weak and winds are strong. A similar fresh bias is seen in the central Pacific Ocean south of 10°S (east of the SPCZ), but $\overline{\Delta S}_{mod}$ is near zero. The fresh bias is strong throughout the western Pacific warm pool in $\overline{\Delta S}_{hyc}$ and in $\overline{\Delta S}_{mod}$ but not in $\overline{\Delta S}_{obs}$. These differences warrant further study.

6. Summary and Discussion

It is shown here that in cases where horizontal advection can be neglected, a one-dimensional turbulence closure model can accurately describe the evolution of the upper ocean during rainfall. Sensitivity experiments demonstrated that the magnitude of the near-surface vertical salinity gradient produced by rain events is linearly related to R and inversely proportional to U. Fitting the idealized fresh lenses gave a coefficient of 0.11 psu (mm h^{-1})$^{-1}$ between ΔS_{max} and R_{max}, consistent with the observational estimates made by Drucker and Riser [2014] and *Boutin et al*. [2014].

The relationships between ΔS, R, and U developed using model results compared reasonably well to the same relationships observed from measurements of around 100 rain events observed at the SPURS mooring. This provides evidence that GOTM does a reasonable job at simulating the upper ocean response to rainfall, and that in many cases one-dimensional dynamics are appropriate for describing the first-order features of rain-formed fresh lenses. The discrepancies between model and observations most likely arise because the near-surface ocean is not an idealized one-dimensional water column: horizontal advection and diffusion, along with vertical entrainment, all affect the formation and evolution of fresh lenses. This becomes increasingly important as the surface fresh anomalies propagate downward: gradients near the surface are likely produced immediately after the rain starts falling, whereas it may take tens of minutes or hours for the anomalies to reach 2 m depth, during which time horizontal advection and diffusion are more likely to affect the evolution of the vertical gradient.

Because salinity anomalies depend strongly on both R and U, detailed studies of the upper ocean response to rain events require accurate observations of both rain and wind speed. Moreover, because tropical rain events are typically brief, have a small spatial extent, and are inhomogeneous with respect to space and time, characterizing their impacts requires collocated, contemporaneous meteorological, and ocean observations. It is also likely that full understanding of the formation and evolution of these fresh lenses will require measurements that characterize both the vertical and horizontal processes, especially within the upper few meters of the mixed layer.

Yearlong GOTM simulations forced by observed rainfall and reanalysis atmospheric variables suggest that in rainy, low-wind regions, persistent fresh lenses can produce mean salinity differences between depths of 0.01 and 5 m on order of −0.1 to −0.2 psu in several ocean regions: the eastern equatorial Indian Ocean west of Sumatra, throughout the western Pacific warm pool, the Pacific and Atlantic ITCZ regions, and the SPCZ. Both the magnitude of this signal and the spatial patterns are largely consistent with biases observed between Aquarius and Argo salinities, and between Aquarius and HYCOM salinities. This suggests that strong and long-lasting fresh lenses may contribute significantly to the fresh bias in these regions. This finding can be compared to the results of Drucker and Riser [2014], who estimated that rainfall contributes a maximum of −0.03 psu to the total Aquarius fresh bias in the tropics. Drucker and Riser [2014] reasoned that rain events are too brief and small in spatial extent to be a significant driver of the bias. In fact, averaging $\overline{\Delta S}_{mod}$ over the 20°S to 20°N domain gives a value of −0.04 psu, consistent with the average value of −0.03 psu found by Drucker and Riser [2014]. However, GOTM allows characterization of the spatial variability of rain impacts, and as is evident from Figures 7a–7c, the domain-averaged value does not represent the regional diversity of vertical salinity gradients. The results from GOTM demonstrate that in order to quantify the impacts of rainfall on satellite-based salinity estimates, it is critical to

consider the spatial variability of rain and wind in more detail than provided by the spatially sparse Aquarius/Argo matched data pairs.

Acknowledgments

We gratefully acknowledge the many sources of publicly available data that were used in this study. The Argo data were collected and made freely available by the International Argo Project and the national programs that contribute to it (http://www.argo.ucsd.edu, http://argo.jcommops.org). Argo is a pilot program of the Global Ocean Observing System. The gridded Argo data were produced by Dean Roemmich and John Gilson at Scripps Institution of Oceanography. The Aquarius SSS data were obtained from the NASA EOSDIS Physical Oceanography Distributed Active Archive Center (PO.DAAC) at the Jet Propulsion Laboratory, Pasadena, CA (http://dx.doi.org/10.5067/AQR40-2SOCS). NOAA provided CMORPH rainfall estimates. J. T. Farrar provided data from the SPURS mooring. ECMWF provided ERA-Interim fields. TAO mooring data were provided by the TAO Project Office of NOAA/PMEL. We thank two anonymous reviewers for their constructive feedback. K.D. acknowledges support from NASA under grant NNX14AQ54GW and from NSF under award number 1458759. W.A. acknowledges support from NASA under grants NNX09AU73G and NNX15AF68G. B.W. and K.W. are grateful for funding support from the Office of Naval Research (award N62909-14-1-N296), and the Norwegian Research Council under the PETROMAKS2 233901 project. Any requests concerning the data in this paper should be directed to the corresponding author.

References

Asher, W. E., A. T. Jessup, R. Branch, and D. Clark (2014), Observations of rain-induced near surface salinity anomalies, *J. Geophys. Res. Oceans*, *119*, 5483–5500, doi:10.1002/2014JC009954.

Boutin, J., N. Martin, G. Reverdin, X. Yin, and F. Gaillard (2013), Sea surface freshening inferred from SMOS and ARGO salinity: Impact of rain, *Ocean Sci.*, *9*(1), 183–192.

Boutin, J., N. Martin, G. Reverdin, S. Morisset, X. Yin, L. Centurioni, and N. Reul (2014), Sea surface salinity under rain cells: SMOS satellite and in situ drifters observations, *J. Geophys. Res. Oceans*, *119*, 5533–5545, doi:10.1002/2014JC010070.

Boutin, J., et al. (2016), Satellite and in situ salinity: Understanding near-surface stratification and sub-footprint variability, *Bull. Am. Meteorol. Soc.*

Brainerd, K., and M. Gregg (1997), Turbulence and stratification on the tropical ocean-global atmosphere-coupled ocean-atmosphere response experiment microstructure pilot cruise, *J. Geophys. Res.*, *102*(C5), 10,437–10,455.

Burchard, H. (2001), Simulating the wave-enhanced layer under breaking surface waves with two-equation turbulence models, *J. Phys. Oceanogr.*, *31*(11), 3133–3145.

Burchard, H., and K. Bolding (2001), Comparative analysis of four second-moment turbulence closure models for the oceanic mixed layer, *J. Phys. Oceanogr.*, *31*(8), 1943–1968.

Burchard, H., K. Bolding, and M. R. Villarreal (1999), GOTM, a general ocean turbulence model: Theory, implementation and test cases, Luxembourg *Rep. EUR 18745*, 103 pp.

Canuto, V., A. Howard, Y. Cheng, and M. Dubovikov (2001), Ocean turbulence. Part I: One-point closure model-momentum and heat vertical diffusivities, *J. Phys. Oceanogr.*, *31*(6), 1413–1426.

Chassignet, E. P., H. E. Hurlburt, O. M. Smedstad, G. R. Halliwell, P. J. Hogan, A. J. Wallcraft, R. Baraille, and R. Bleck (2007), The HYCOM (hybrid coordinate ocean model) data assimilative system, *J. Mar. Syst.*, *65*(1), 60–83, doi:10.1016/j.jmarsys.2005.09.016.

Cheng, Y., V. Canuto, and A. Howard (2002), An improved model for the turbulent PBL, *J. Atmos. Sci.*, *59*(9), 1550–1565.

Clark, N., L. Eber, R. Laurs, J. Renner, and J. Saur (1974), Heat exchange between ocean and atmosphere in the eastern North Pacific for 1961-71, *Tech. Rep. NMFS SSRF-682* NOAA, U.S. Dept. of Commerce, Washington, D. C.

Dee, D., et al. (2011), The ERA-Interim reanalysis: configuration and performance of the data assimilation system, *Q. J. R. Meteorol. Soc.*, *137*, 553–597, doi:10.1002/qj.828.

Drucker, R., and S. C. Riser (2014), Validation of Aquarius sea surface salinity with Argo: Analysis of error due to depth of measurement and vertical salinity stratification, *J. Geophys. Res. Oceans*, *119*, 4626–4637, doi:10.1002/2014JC010045.

Fairall, C. W., E. F. Bradley, D. P. Rogers, J. B. Edson, and G. S. Young (1996), Bulk parameterization of air-sea fluxes for tropical ocean-global atmosphere coupled-ocean atmosphere response experiment, *J. Geophys. Res.*, *101*(C2), 3747–3764.

Farrar, J. T., et al. (2015), Salinity and temperature balances at the SPURS central mooring during fall and winter, *Oceanography*, *28*(1), 56–65.

He, H., and D. Chen (2011), Effects of surface wave breaking on the oceanic boundary layer, *Geophys. Res. Lett.*, *38*, L07604, doi:10.1029/2011GL046665.

Henocq, C., J. Boutin, G. Reverdin, F. Petitcolin, S. Arnault, and P. Lattes (2010), Vertical variability of near-surface salinity in the tropics: Consequences for L-band radiometer calibration and validation, *J. Atmos. Oceanic Technol.*, *27*(1), 192–209.

Jeffery, C., I. Robinson, and D. Woolf (2010), Tuning a physically-based model of the air–sea gas transfer velocity, *Ocean Modell.*, *31*(1), 28–35.

Jerlov, N. G. (1976), *Marine Optics*, Elsevier, Amsterdam.

Joyce, R. J., J. E. Janowiak, P. A. Arkin, and P. Xie (2004), CMORPH: A method that produces global precipitation estimates from passive microwave and infrared data at high spatial and temporal resolution, *J. Hydrometeorol.*, *5*(3), 487–503.

Kantha, L. H., and C. A. Clayson (1994), An improved mixed layer model for geophysical applications, *J. Geophys. Res.*, *99*(C12), 25,235–25,266, doi:10.1029/94JC02257.

Katsaros, K., and K. J. Buettner (1969), Influence of rainfall on temperature and salinity of the ocean surface, *J. Appl. Meteorol.*, *8*(1), 15–18.

Lindstrom, E., F. O. Bryan, and R. W. Schmitt (2015), SPURS: Salinity processes in the upper-ocean regional study—The North Atlantic experiment, *Oceanography*, *28*(1), 14–19.

McCulloch, M., P. Spurgeon, and A. Chuprin (2012), Have mid-latitude ocean rain-lenses been seen by the SMOS satellite?, *Ocean Model.*, *43*, 108–111, doi:10.1016/j.ocemod.2011.12.005.

Meissner, T., F. Wentz, J. Scott, and K. Hilburn (2014), Upper ocean salinity stratification and rain freshening in the tropics observed from Aquarius, in *IEEE International Geoscience and Remote Sensing Symposium (IGARSS)*, pp. 5111–5114, IEEE. Québec City, Canada.

Mellor, G. L. (1989), Retrospect on oceanic boundary layer modeling and second moment closure, in *Parameterization of Small-Scale Processes, Proceedings of the Aha Hulikoa Hawaiian Winter Workshop*, pp. 251–271, Univ. of Hawaii at Manoa, Honolulu.

Mellor, G. L., and T. Yamada (1982), Development of a turbulence closure model for geophysical fluid problems, *Rev. Geophys.*, *20*(4), 851–875, doi:10.1029/RG020i004p00851.

Paulson, C. A., and J. J. Simpson (1977), Irradiance measurements in the upper ocean, *J. Phys. Oceanogr.*, *7*(6), 952–956.

Pimentel, S., K. Haines, and N. Nichols (2008), Modeling the diurnal variability of sea surface temperatures, *J. Geophys. Res.*, *113*, C11004, doi:10.1029/2007JC004607.

Price, J. F. (1979), Observations of a rain-formed mixed layer, *J. Phys. Oceanogr.*, *9*(3), 643–649.

Reed, R. (1977), On estimating insolation over the ocean, *J. Phys. Oceanogr.*, *7*(3), 482–485.

Reverdin, G., S. Morisset, J. Boutin, and N. Martin (2012), Rain-induced variability of near sea-surface T and S from drifter data, *J. Geophys. Res.*, *117*, C02032, doi:10.1029/2011JC007549.

Rodi, W. (1987), Examples of calculation methods for flow and mixing in stratified fluids, *J. Geophys. Res.*, *92*(C5), 5305–5328.

Roemmich, D., and J. Gilson (2009), The 2004–2008 mean and annual cycle of temperature, salinity, and steric height in the global ocean from the Argo Program, *Prog. Oceanogr.*, *82*(2), 81–100.

Santos-Garcia, A., M. M. Jacob, W. L. Jones, W. E. Asher, Y. Hejazin, H. Ebrahimi, and M. Rabolli (2014), Investigation of rain effects on Aquarius sea surface salinity measurements, *J. Geophys. Res. Oceans*, *119*, 7605–7624, doi:10.1002/2014JC010137.

Smyth, W., P. Zavialov, and J. Moum (1997), Decay of turbulence in the upper ocean following sudden isolation from surface forcing, *J. Phys. Oceanogr.*, *27*(5), 810–822.

Soloviev, A., and R. Lukas (1996), Observation of spatial variability of diurnal thermocline and rain-formed halocline in the western pacific warm pool, *J. Phys. Oceanogr.*, *26*(11), 2529–2538.

Soloviev, A., and R. Lukas (2006), *The Near-Surface Layer of the Ocean: Structure, Dynamics and Applications, Atmospheric and Oceanographic Sciences Library*, vol. 31, 574 pp., Springer, Dordrecht, Netherlands, doi:10.1007/1-4020-4053-9.

Soloviev, A., R. Lukas, and H. Matsuura (2002), Sharp frontal interfaces in the near-surface layer of the tropical ocean, *J. Mar. Syst.*, *37*(1), 47–68.

Soloviev, A. V., S. Matt, and A. Fujimura (2015), Three-dimensional dynamics of freshwater lenses in the ocean's near-surface layer, *Oceanography*, *28*(1), 142–149.

SPURS-2 Planning Group (2015), From salty to fresh–salinity processes in the Upper-ocean Regional Study-2 (SPURS-2): Diagnosing the physics of a rainfall-dominated salinity minimum, *Oceanography*, *28*(1), 150–159, doi:10.5670/oceanog.2015.15.

Stips, A., H. Burchard, K. Bolding, and W. Eifler (2002), Modelling of convective turbulence with a two-equation k-ϵ turbulence closure scheme, *Ocean Dyn.*, *52*(4), 153–168.

Tang, W., S. H. Yueh, A. G. Fore, and A. Hayashi (2014), Validation of Aquarius sea surface salinity with in situ measurements from Argo floats and moored buoys, *J. Geophys. Res. Oceans*, *119*, 6171–6189, doi:10.1002/2014JC010101.

Tomczak, M. (1995), Salinity variability in the surface layer of the tropical western Pacific Ocean, *J. Geophys. Res.*, *100*(C10), 20,499–20,515.

Umlauf, L., and H. Burchard (2003), A generic length-scale equation for geophysical turbulence models, *J. Mar. Res.*, *61*(2), 235–265.

Walesby, K., J. Vialard, P. Minnett, A. Callaghan, and B. Ward (2015), Observations indicative of rain-induced double diffusion in the ocean surface boundary layer, *Geophys. Res. Lett.*, *42*, 3963–3972, doi:10.1002/2015GL063506.

Ward, B., T. Fristedt, A. H. Callaghan, G. Sutherland, X. Sanchez, J. Vialard, and A. ten Doeschate (2014), The Air-Sea Interaction Profiler (ASIP): An autonomous upwardly-rising profiler for microstructure measurements in the upper ocean, *J. Atmos. Oceanic Technol.*, *31*, 2246–2267, doi:10.1175/JTECH-D-14-00010.1.

Webster, P. J., C. A. Clayson, and J. A. Curry (1996), Clouds, radiation, and the diurnal cycle of sea surface temperature in the tropical western Pacific, *J. Clim.*, *9*(8), 1712–1730.

Wijesekera, H., C. Paulson, and A. Huyer (1999), The effect of rainfall on the surface layer during a westerly wind burst in the western equatorial pacific, *J. Phys. Oceanogr.*, *29*(4), 612–632.